Polymorphism with Conformational Isomerism and Incomplete Crystallization in Solid Ethanolamine

*Michela Romanini,[1,†] Philippe Negrier,[2] Pragya Tripathi,[1] Kyriaki-Marina Lira,[3] Dimitrios Gournis,[3] Maria Barrio,[1] Luis Carlos Pardo,[1] Josep Lluís Tamarit,[1] Roberto Macovez[1,]**

[1] Grup de Caracterització de Materials, Departament de Física, and Barcelona Research Center in Multiscale Science and Engineering, Universitat Politècnica de Catalunya, EEBE, Campus Diagonal-Besòs, Av. Eduard Maristany 10-14, 08019 Barcelona, Catalonia, Spain.

[2] Université Bordeaux, LOMA, UMR 5798, F-33400 Talence, France CNRS, LOMA, UMR 5798, F-33400 Talence, France

[3] Department of Materials Science and Engineering, University of Ioannina, 45110 Ioannina, Greece

* Corresponding author. Tel: +34 934016568. E-mail: roberto.macovez@upc.edu.

ABSTRACT. We employ calorimetry, Rietveld refinement of X-ray powder diffraction, broadband dielectric spectroscopy and molecular dynamics simulations, to investigate the phase behavior, crystal structure, dc conductivity and dielectric response of the condensed phases of ethanolamine (EAM), an ethane derivative with two distinct hydrogen-bonding groups. EAM is found to exhibit, besides its stable crystal phase, a metastable crystalline phase obtained from the supercooled liquid phase. The metastable phase can only be maintained at low temperature; upon heating an irreversible exothermic transformation to the stable crystal structure takes place at 210 K, with a low transition enthalpy of ca. 2.4 J/g. The observed polymorphism is accompanied by differences in the molecular conformation and degree of structural order. Each EAM molecule participates in six H-bonds in both crystalline phases. While the stable phase is fully ordered, the metastable phase appears to be characterized by a statistical disorder in the position of the hydrogen atoms and thus of the intramolecular conformation and intermolecular hydrogen bonding. Our molecular dynamics simulations suggest that such disorder is dynamic in character, and allow analyzing the dynamic H-bonding motif of the metastable phase in terms of composition, length and energy of the H-bonds, and molecular conformations involved. Charge conduction is mainly ionic in both crystalline phases and exhibits the typical temperature dependence of disordered solid electrolytes, rather than crystalline ones. Dielectric characterization indicates that, upon crystallization of liquid EAM, a small fraction of the sample (approximately 5%) remains amorphous, a situation similar to that reported for other H-bonded systems such as glycerol and *n*-butanol.

KEYWORDS: ethane derivative; metastable crystal phase; Rietveld refinement; molecular dynamics; hydrogen bond network; frustrated crystallization

1. Introduction

Hydrogen bonding is responsible for a number of important effects in condensed matter. The importance of H-bonds in liquid aqueous media is notorious, as they determine the anomalous density behavior, solvation power, and proton transfer properties of water,[1,2] and are a fundamental ingredient for protein folding[3] and molecular recognition.[4] Perhaps less celebrated is the fact that hydrogen bonding is equally important also for the solid state properties of many organic systems.[5,6] For example, extensive hydrogen bonding is responsible for the large molecular dipole moments of biopolymers (*e.g.*, DNA helices), and play a fundamental role for the piezoelectricity and ferroelectricity of order-disorder ferroelectric materials;[7,8] the first piezoelectric material ever to be identified was in fact a H-bonded hydrate salt.[9] If the H-bond network is dynamic, it can result in a particular type of charge transport, known as proton exchange or Grotthuss mechanism, which is for example responsible for the relatively high dc conductivity of ice as well as that of water[10,11] and of some hydrates and water clathrates,[12] and for the conductivity enhancement of low-conductivity materials upon condensation of water vapor.[13,14]

The impact of H-bond interactions is particularly important from a structural perspective. It is known, for example, that the morphology and structure of crystals grown from aqueous or alcohol solutions depend on the H-bond interaction motif within the clusters of the saturated solvent.[15] For pure organic species capable of H-bonding, this highly directional interaction is a crucial factor in determining the polymorphism of the material,[16-18] to the point that it can be exploited to achieve crystal engineering, the controlled design of molecular and supramolecular crystal structure.[19] This is normally achieved using molecular recognition schemes with carefully designed molecular constituents.

In the case of flexible hydrogen-bonding molecules, polymorphism can result from the interplay of two factors: the existence of competing conformers of the same molecule, and their different capability for H–bond formation. In this contribution, we analyze the effect of hydrogen bonding and multiple molecular conformations on the crystal structure and H–bond dynamics of one of the simplest flexible organic molecule, ethanolamine (C_2H_7NO), a biologically important ethane derivative (it is the second most-abundant head group of phospholipids) which is used as feedstock of organic and pharmaceuticals products as well as an absorber for the capture of CO_2 emissions in industrial processes and plants.[20,21] Di-substituted ethane derivatives are the simplest non-rigid molecules capable of H–bond formation, and ethanolamine in particular is the simplest molecule that can form an intramolecular H–bond.[22] In terms of possible molecular conformations, ethanolamine (EAM) is a three-rotor molecule, where one rotation is around the C–C bond, and two more rotational degrees of freedom correspond to the internal rotation of the –OH and $–NH_2$ groups. For any value of the dihedral angle defined by the position of the oxygen and nitrogen moieties (N–C–C–O), three distinct rotational states exist, leading to a total of $3^3 = 27$ distinct staggered EAM conformations (with 14 energetically non-equivalent configurations).[23]

Compared with other H-bonding molecular species, EAM is not only flexible and characterized by a richer variety of conformations, but also, it can form extended H–bond networks with a density of three bonds per molecule[24] (for comparison, H_2O can form at the most two H-bonds per molecule). Moreover, while in systems such as water or polyalcohols all H–bonds have the same chemical composition (O···H–O) with a proton being partially shared between two homonuclear moieties, EAM possesses two different H-bonding groups, namely an amine group ($–NH_2$) and a hydroxyl group (–OH), and can therefore form a larger variety of H-bond structures.

The main experimental tools that we employ are temperature-dependent X-ray powder diffraction and broadband dielectric spectroscopy, which we complement with molecular dynamics simulations. We find that EAM can crystallize in two different solid phases; in particular, a metastable crystalline phase is obtained by rapidly cooling the EAM liquid. The metastable phase displays different conformational isomers and a different H–bonding motif than the stable solid phase,[24] and likely by a statistical disorder of the H-bonds. A home-developed software allows us to extract from our molecular dynamics simulations bond length and angles and intermolecular interaction energies. By means of dielectric spectroscopy we observe that EAM displays ionic conduction typical of disordered electrolytes and that crystallization from the liquid phase is only partial, with approximately 5% of the sample that does not undergo crystallization and remains in a supercooled liquid state. Such "frustrated" crystallization might be a consequence of the competing H-bond schemes responsible for the polymorphism of EAM.

2. Materials and Methods

Ethanolamine (EAM) was purchased from BDH Chemicals ltd (Merck) with 99% purity, and used as received. We characterized EAM by temperature-dependent differential scanning calorimetry (DSC), X-ray powder diffraction (XRPD), and broadband dielectric spectroscopy (BDS). During DSC and XRPD experiments, as detailed below, we found that EAM displays both a stable and a metastable crystalline form (see Section 3). The metastable crystalline form was obtained by fast-cooling (approximately at 10 K min^{-1}) the liquid below the melting point (283 K). The stable form was obtained either by slow cooling the liquid to just below the crystallization temperature, between 260 and 270 K depending on the cooling rate, or by reheating the metastable phase to above 230 K.

DSC measurements were carried out with two calorimeters from TA-Instruments, one (Q100) equipped with an intracooler system operating down to 190 K, and the other (TA 2920) equipped with a liquid nitrogen cryosystem operating down to 110 K. The heating/cooling rate was set to 10 K min^{-1}. The samples were weighed before and after the measurements with a microbalance sensitive to 0.01 mg.

For XRPD measurements, liquid EAM was inserted into a Lindemann capillary of 0.5 mm diameter and a similar thermal treatment was applied to obtain the stable and metastable phases. High-resolution XRPD profiles were recorded with a vertically mounted INEL cylindrical position-sensitive detector (CPS120). The generator voltage and current were set to 35 kV and 35 mA, and Cu $K\alpha_1$ radiation (λ = 1.54056 Å) was selected with a Ge(111) monochromator. The detector was used in transmission mode with 2θ angular step of 0.029º, and each diffraction pattern was obtained by measuring during roughly one hour.

The structure of the metastable crystalline phase obtained from the Rietveld refinement of the XRPD data was fed into a molecular dynamics (MD) simulation software (Gromacs v5.0.2)[25] where each molecule was modeled using the semi-flexible OPLS (Optimized Potentials for Liquid Simulations) Force Field,[26,27] which was shown[28] to best reproduce some macroscopic properties such as density, enthalpy of vaporization and the dielectric spectra in the time window accessible for MD. A crystal with the metastable structure and containing 490 molecules was produced using the symmetries obtained by the Rietveld refinement. The metastable phase was simulated during 200 picoseconds in an NVT ensemble at T = 100 K, in order to assess its stability and the compatibility of the Force Field parameters employed with the experimental results. The temperature at which the metastable phase could be maintained stable in our simulations was lower than the one found experimentally. The home-developed software[29] ANGULA was employed to

analyze the H–bond geometry and strength. For the identification of the molecules in closest contact we determined the surface-surface distance distribution function, a probability distribution function representing the minimum distances between each pair of molecules.

For dielectric measurements, liquid EAM was placed at room temperature inside home-made stainless steel parallel-plate capacitors designed for measuring liquid samples in the radiofrequency and microwave ranges. The capacitor was then loaded in a nitrogen-gas cryostat for temperature control. Isothermal dielectric spectra were measured between 10^{-1} and 10^{9} Hz, at several fixed temperatures in the temperature range between 120 and 303 K (with a temperature stability better than ±0.3 K). For measurements between 10^{-1} to $5 \cdot 10^{6}$ Hz a Novocontrol Alpha analyzer was employed, connected to a parallel-plate capacitor via electrical contacts; for measurements in the range from 10^{6} to 10^{9} Hz, a HP4291 impedance analyzer was employed, with the sample capacitor mounted at the end of a coaxial cable in reflectometry geometry. In both cases the two electrode plates were kept separated by needle-like cylindrical silica spacers of 50 μm diameter.

BDS is a versatile technique that allows studying with a single experimental setup both the charge transport and polarization dynamics of condensed matter samples.[30,31] The isothermal dielectric spectra are complex functions of frequency that can be displayed in several representations, for example as complex relative permittivity $\varepsilon_r = \varepsilon' - i\varepsilon''$ (consisting of the dielectric function $\varepsilon'(f)$ and the loss spectrum $\varepsilon''(f)$) and as complex conductivity, defined in the Novocontrol data acquisition program as $\sigma = i2\pi f\varepsilon_0(\varepsilon_r - 1)$ (of which the real part, $\sigma'(f) = 2\pi f\, \varepsilon_0\, \varepsilon''(f)$, is the ac conductivity spectrum).[32]

The low- and high-frequency permittivity spectra at a given temperature can be merged into a single spectrum covering the whole experimentally available frequency range, by rescaling the

spectra acquired with the high-frequency spectra so as to match the values of the real or imaginary permittivity of the spectra acquired with the low-frequency setup.[33] The resulting ε"(*f*) spectra (or equivalently, the σ'(*f*) spectra) were fitted as the sum of one or two relaxation processes (depending on the phase), each modeled as the imaginary part of a Cole-Cole function, and a background representing the dc conductivity (σ_{dc}) contribution. The analytical expression of the Cole-Cole equation is:[34]

(Eq. 1) $\varepsilon_{CC}(f) = \varepsilon_\infty + \frac{\Delta\varepsilon}{1+(i2\pi f\tau)^c}$

Here, $\Delta\varepsilon = \varepsilon_s - \varepsilon_\infty$ is the dielectric strength (equal to the step variation of the real part of the permittivity ε'), and ε_∞ and ε_s are the high-frequency and low-frequency (static) limits of ε'(*f*), respectively. τ is the so-called "relaxation time", at which the dielectric loss is maximum, and the exponent *c*, which lies in the range from 0 to 1, is related to the width of the relaxation feature in the loss spectrum. The Cole-Cole equation is a phenomenological generalization of the Debye function, which corresponds to the special case *c* = 1 in Eq. 1.

3. Results and Discussion

3.1 Phase Transitions in EAM and Analysis of the Metastable and Stable Crystal Structures

The 27 conformers of EAM can be classified in two general groups as *trans* or *gauche* according to the N–C–C–O dihedral angle. EAM displays different conformations in different phases, due also to the presence of hydrogen-bonding groups (–OH and $–NH_2$) leading to relatively strong intramolecular or intermolecular interactions. For example, in the gas phase where intermolecular interactions are negligible, the stable form of EAM is a *gauche* conformer with an intramolecular O–H···N bond between the two polar groups of the same molecule.[22,35] At room temperature, EAM is a highly polar liquid, with relative dielectric constant ε_r of approximately 30. The local structure

and the relative population of different conformers in liquid EAM are still debated,[36,37] but the general consensus is that the majority of EAM molecules are in (twofold degenerate) *gauche* conformations and a minority are in a *trans* conformation, and most H-bonds are intermolecular bonds involving N and O moieties (rather than intramolecular as in the gas phase). When EAM is dissolved in other organic solvents, the *gauche* conformers are found to be energetically favored regardless of the solvent polarity.[38] Finally, in the stable solid phase, of monoclinic symmetry, the molecules are in the more open *trans* conformation, with each molecule participating in six hydrogen bonds both of the O···H–N and N···H–O types.[24]

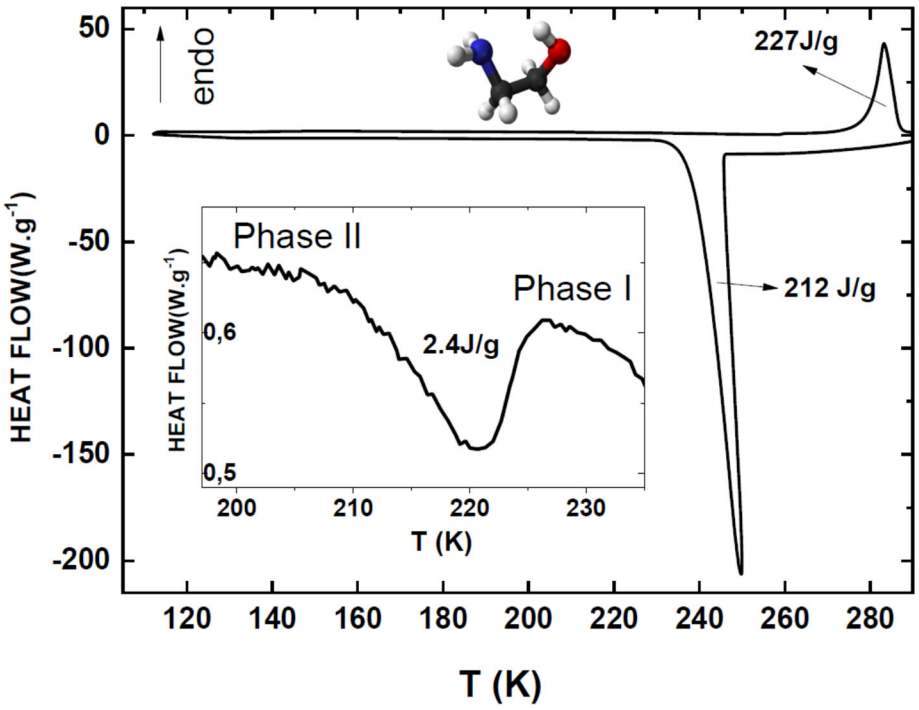

Figure 1. Calorimetry thermogram acquired by cooling liquid EAM from room temperature at a rate of 10 K min^{-1} to 110 K, and subsequently heating the sample to room temperature. Inset: zoom-in of the solid-solid transition observed upon heating.

Figure 1 shows the DSC thermograms acquired upon fast-cooling liquid EAM down to 110 K and subsequently heating the sample above the melting point of the monoclinic *Cc* stable crystal phase (labeled as phase I). On cooling, crystallization is observed as a sharp exothermic peak with onset at 250 ± 1 K. On heating, a second exothermal process is observed at 210 ± 1 K (onset point), as visible in the inset to Figure 1, which corresponds to an irreversible solid-solid transition between a metastable phase II and the stable phase I, as evidenced by the observation of the melting peak temperature at 283 K (with onset at 280 ± 2 K).[39] According to our temperature-dependent X-ray diffraction results (Figure 2), the low temperature phase II obtained by rapid cooling from the liquid has its own characteristic diffraction pattern, which changes into a different pattern as the temperature is raised across the irreversible phase transition (see below).

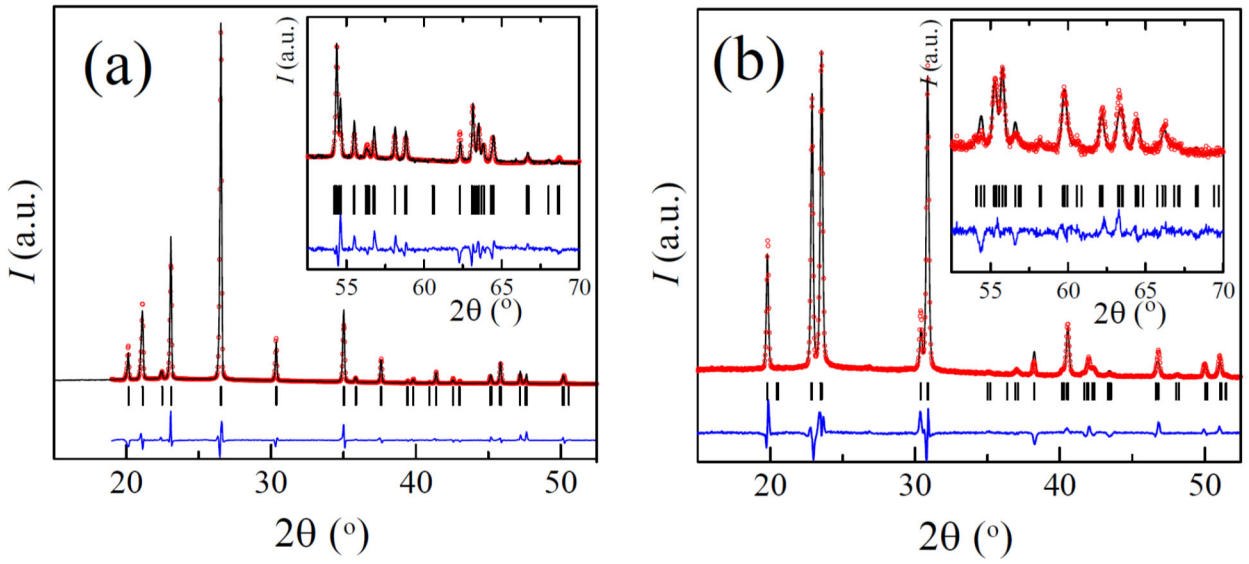

Figure 2. Experimental XRPD patterns (red circles) of the stable Phase I at 250 K (a) and of the metastable Phase II at 100 K (b), and comparison with the results of the Rietveld refinement (black lines) along with the difference profile (blue line) and Bragg reflections (vertical black sticks). The

inset provides the data between 52.5 and 70° (2θ) at an increased y-scale (factor 17 for (a) and 13 for (b))

Table 1. Lattice parameters of the metastable and stable phases.

solid phase	T / K	crystal system	space group	Z	a / Å	b / Å	c / Å	β / º
Stable (I)	250	monoclinic	Cc	4	5.0195(8)	8.8181(16)	8.3076(11)	107.726(8)
Metastable (II)	100	monoclinic	$P2_1$	2	5.0947(18)	7.7762(19)	4.9312(15)	118.638(12)

To identify the structure of phase II, we carried out a Rietveld refinement of the XRPD pattern recorded at 100 K with a long acquisition time. The lattice and the possible space groups of phase II were determined at 100 K by means of X-Cell software, through the module Powder Indexing of Materials Studio,[40] assuming similar density to the stable phase I. A further Pawley refinement minimizing the weighted *R*-factor, R_{wp}, confirmed the initial indexing result and, in addition, provided the systematic absences for the space group assessment, compatible with $P2_1$ and $Z = 2$. In order to determine the structure of phase II we built up the molecule of EAM using the geometry proposed for the stable phase I,[24] but allowing for different positions of the H atoms of the functional groups to be occupied with a statistical probability factor. Rietveld refinement of the orientation and position of the molecule, together with a single overall isotropic displacement and preferred orientation by using the March-Dollase function, provides a satisfactory solution according to the weighted R-factors (R_p = 6.91%, R_{wp} = 10.17%). Final Rietveld parameters are gathered in Table 1, and the refined pattern together with the experimental pattern is depicted in Figure 2(b). The CIF files of the stable and metastable phase are provided as separate files. We point out that we also carried out a refinement without statistical disorder; such refinement gave a fully ordered structure with, however, intermolecular H–H distances that were too short to be

compatible with the steric repulsion between the molecules. There are other organic molecules, that similarly display a fully ordered stable crystal phase and a partially disordered metastable crystal phase; one example is 2-adamantanone.[41,42] The fact that phase II is disordered, while phase I is fully ordered, and that the transition from phase II to phase I is irreversible, evidence the monotropic behavior of the metastable phase II with respect to the stable phase I.

In order to contrast the refinement of the metastable phase, an identical procedure (without statistical disorder) was followed for phase I, whose result is shown in Figure 2(a). Weighted factors (R_p = 7.01% and R_{wp} = 10.44%) are quite similar and the refined lattice parameters (see Table 1) are virtually the same than those previously obtained from single crystal diffraction.[24] Figure 3 depicts the structures of stable and metastable phases, seen along two different crystallographic directions. Both crystal structures belong to the monoclinic crystal system, with only one independent molecule in both structures (Z' = 1). In both phase I and phase II all the molecules have a *trans* overall conformation with a dihedral N–C–C–O angle of 180º. The most relevant differences between the two structures are the slightly different conformational angles and spatial arrangement of the molecular side groups, and the existence, in the metastable phase, of a statistical disorder for both the amine and hydroxyl groups, both with occupancy rates of 0.5.

In the stable phase all EAM molecules are in the same conformation, which can be written as *g'Tg*, where the capital *T* stands for the fact that all conformers are of the general *trans* type while the small *g*'s indicate the possible positions of the lone pair of the nitrogen atom (left *g* symbol) and of the hydroxyl hydrogen (right *g* symbol) with respect to the C–N or C–O bond, respectively.[37] In the stable phase the angles formed by the covalent N–H bonds with respect to the C–N bonds are 105.9º (C1–N1–H2) and 100.7º (C1–N1–H3), respectively, and the C–O–H angle is 117.3º. By comparison, in the metastable phase, the C–O–H angle is 105.5º for either

possible position of the hydrogen moiety, and the C–N–H bond is 107.6º, virtually independent of the positions of the H moiety. Different possible molecular conformations are present in the metastable phase, which we discuss in what follows in relation to the H-bond motif of the metastable phase II.

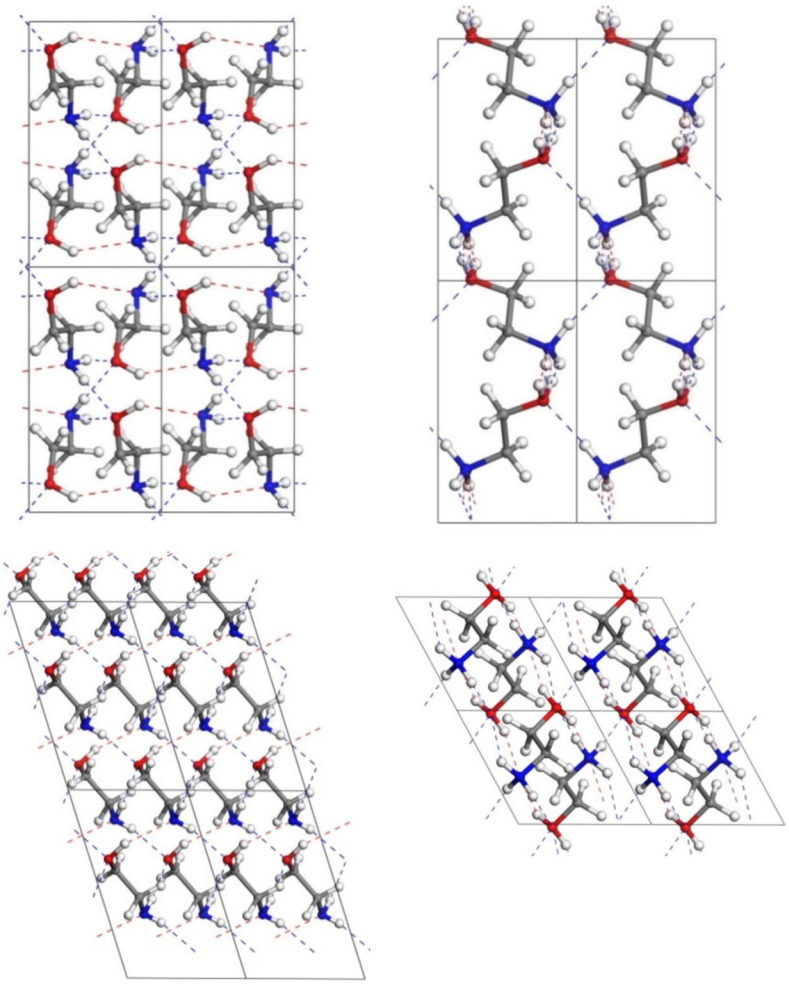

Figure 3. Crystal structures of the stable Phase I at 250 K (left panels) and metastable Phase II at 100 K (right panels) along *c* (upper panels) and along *b* (lower panels). Dashed lines indicate the hydrogen O···H–N (blue) and O···H–N (red) bonds.

As reported in the literature,[24] in the stable phase short O···H–N bonds (2.019 Å) form zig-zag chains within the *ac* plane, while weaker O···H–N and N···H–O bonds (2.266 and 2.330 Å) link each molecule in such a chain with the four closest neighbor molecules (in nearby chains). The metastable phase II exhibits a similar bonding scheme, but with only strong O···H–N bonds and weak N···H–O ones. The occupational disorder of the hydrogen atom (labeled as H41 and H42 in the CIF file) within the metastable phase II shortens the H–bond (N···H–O) distance between H and the N atoms (2.184 Å and 1.888 Å for H41 and H42, respectively), while within the hydrogen bonding scheme for stable phase I such bond distance is 2.330 Å. As for the former, O···H–N, the distances between H and O atoms account for 2.266 and 2.019 Å within phase I, and 2.078, 2.234 and 1.815 Å (for H31, H32 and H33, respectively). In both phases, each molecule participates in a total of 6 H–bonds, which is the maximum number of strong or moderate intermolecular bonds that an EAM molecule can form; all H–bonds are heteronuclear, while no homonuclear bonds are formed.

In order to determine whether the observed statistical disorder of the metastable phase II is static or dynamic in character, and in the latter case, to study the resulting H–bond distribution, the refined structure of the metastable crystal phase II was taken as starting point for a molecular dynamics (MD) simulation (the stable phase is instead, as mentioned, fully ordered). The total interaction energy of a pair of first neighbor molecules was calculated using the Force Field employed for the MD simulations, which was shown[28] to best reproduce macroscopic properties of liquid EAM such as density and enthalpy of vaporization. We have also employed the same Force Field to run a series of MD simulations of the stable phase I in the NVT ensemble, taking as starting point the structure obtained for our Rietveld refinement (which as mentioned coincides with the structure obtained in an earlier single-crystal diffraction study[24]). No phase transition was

observed in these simulations, which indicates that the Force Field of Ref. **¡Error! Marcador no definido.** is applicable also for solid EAM.

The MD trajectories obtained for the metastable phase II were analyzed with a home-developed program (ANGULA)[29] to extract statistical information about the geometry and strength of nearest-neighbor molecular interactions. Figure 4(a) shows the energy-distance maps in phase II, calculated as a bivariate probability distribution. The position of the spots in the map gives information about the energy of the molecular contacts, and their intensity (scale of blue) is proportional to the number density of a particular bond. It is seen that the two types of (heteronuclear) hydrogen bonds in the metastable phase have quite different strengths. In particular, the two N···H–O bonds have higher contact energy of about 6.3 kJ mol^{-1}, while the four O···H–N bonds have lower contact energy of 3.5 to 5 kJ mol^{-1}. The latter bonds could be subdivided in two groups with different contact energy: two O···H–N bonds display relatively shorter distance and larger interaction energy (4 kJ mol^{-1}), and the other two a larger distance and a correspondingly weaker interaction energy (3 kJ mol^{-1}).

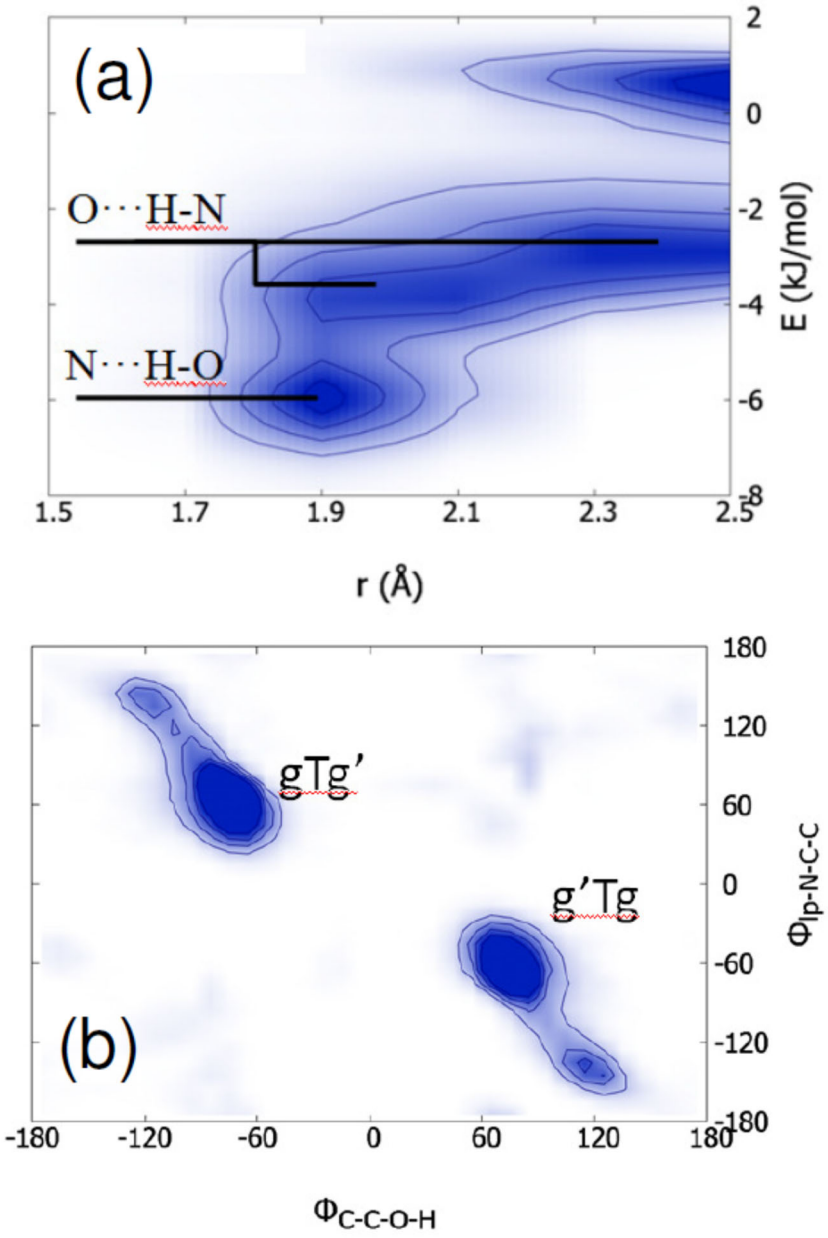

Figure 4. Results of MD simulations on the metastable solid phase II of EAM. (a) Statistical contour plots (distance-energy maps) of the nearest-neighbor interaction. The most probable values for distance and energy for two molecules are shown as colored spots. The horizontal axis represents the shortest intermolecular distance (r) in Å, while the vertical axis represents the total energy of interaction in kJ mol^{-1}. A value of the interaction (contact) energy between –3 and –7 kJ mol^{-1} was taken to be an indication of the presence of a mild to strong H-bond between two

molecules. (b) Bivariate probability distribution function of the dihedral $\Phi_{C\text{-}C\text{-}O\text{-}H}$ and $\Phi_{lp\text{-}N\text{-}C\text{-}C}$ angles defining the relative orientation of the hydroxyl group and of the nitrogen lone pair (lp) of an EAM molecule.

The fact that the contour map of Figure 4(a) is rather diffuse, instead of consisting of well definite spots, reflects the existence of a dynamic structural disorder in the metastable phase, which is observed in our MD simulations. The intramolecular conformations (*i.e.*, the three dihedral angles defining the molecular geometry) are in fact accessible for the MD trajectories, which allows investigating if there is any conformational disorder and identifying the most probable molecular configurations in the metastable phase II. We follow the nomenclature of Ref. 37, whereby the symbols *kLm* represent the *trans* or *gauche* configuration for the orientation of the lone electron pair of the NH_2 group, the backbone (N–C–C–O), and the OH group, in this order. For gauche orientations we distinguish between the dihedrals close to 60º (*g*) and those close to –60º (*g'*). As it can be seen in Figure 4(b), in the metastable phase both NH_2 and OH groups can be either in g or g' configuration. However, there is a correlation between the two possible configurations, such that when the lone pair (lp) on the nitrogen is in the *g'* configuration, the hydroxyl group is in the *g* configuration, and *viceversa*. From the figure we can also observe the route followed by the molecules to change conformation: the spots located at ±120º for both groups of conformers indicate that the conformational change always takes place by a rotation which avoids the energetically disfavored *t* configuration.

3.2. Electric Conductivity and Dielectric Relaxations in EAM

Figure 5(a) shows the isothermal ac conductivity spectra σ'(*f*) of a solid EAM sample obtained by fast cooling from the liquid phase to 120 K. The spectra were measured upon heating every 2

K, increasing the temperature in a stepwise fashion form 120 K to room temperature. All spectra display a plateau-like region, corresponding to the dc value of the conductivity (σ_{dc}), which shifts to higher frequency with increasing temperature due to the electrode polarization effect (decrease of σ' at the low-frequency side of the dc plateau). The sequence of spectra highlights the presence of two major phase changes, visible as sudden jumps in the σ_{dc} value. Such discontinuities are best visualized in the Arrhenius plot presented in Figure 5(b), which also displays the dc conductivity values of the stable phase at low temperature. The first phase change occurs (upon heating) in the temperature range between 219 and 229 K, which corresponds to the range of the solid-solid transition between the metastable and the stable phases observed by DSC (inset to Figure 1). The other phase change visible in Figure 6 is the melting of the stable crystal phase, between ca. 277 and 281 K. Upon melting, σ_{dc} increases by roughly two orders of magnitude.

The dc conductivity Arrhenius plots of both the metastable and stable solid phases exhibit a negative curvature (sub-Arrhenius behavior) at low temperature. This negative curvature is typical of ionic conduction in disordered phases such as polymers and plastic crystals.[31,43] The observation of ionic conductivity is an interesting finding for a crystalline phase, as not many ordered solids behave as ionic conductors. It is interesting to note that the ionic conductivity of the stable crystal is higher than that of the metastable one by one or two orders of magnitude depending on the temperature, despite the presence of a dynamic disorder in the metastable phase, which should in principle be beneficial to ion diffusion. This makes it unlikely that the charge transport in solid EAM involves the Grotthus proton shuttling typical of water and hydrated samples;[13,14,44,45] the ionic conductivity of EAM should be rather ascribed to diffusion of ionic species.

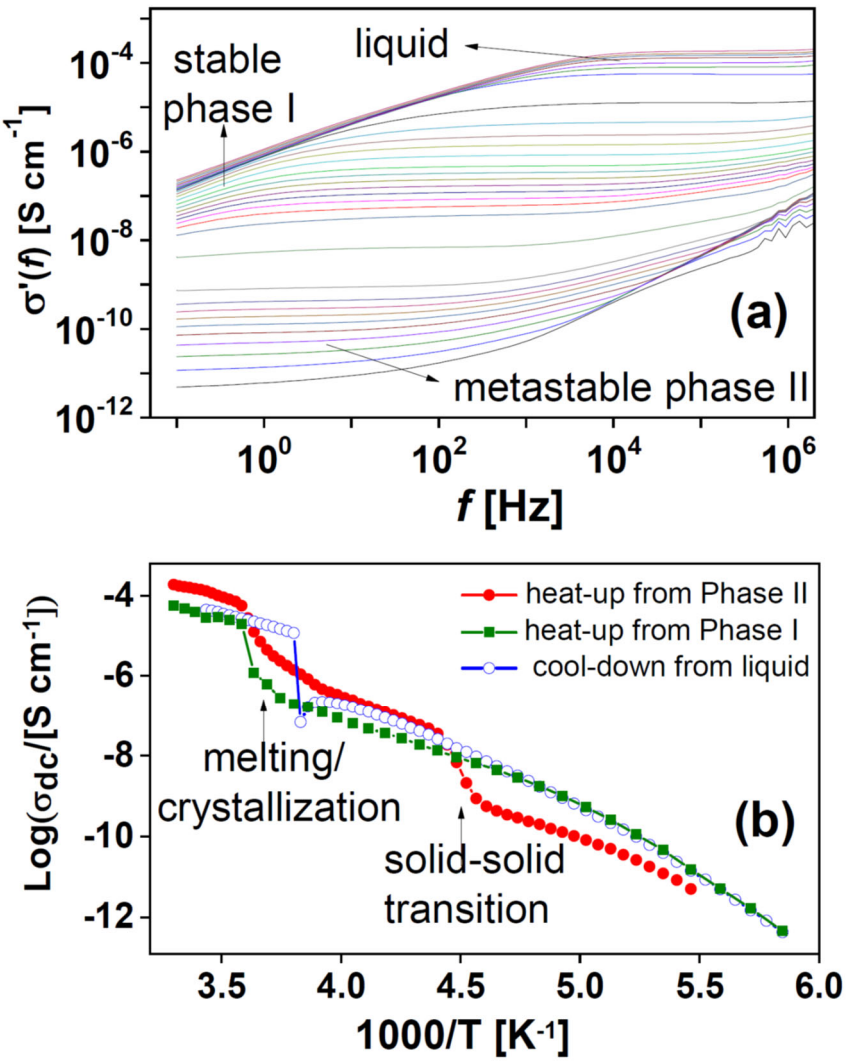

Figure 5. Isothermal ac conductivity spectra of EAM between 183 and 303 K every 4 K, measured by increasing the temperature in steps of 2 K. The grouping of spectra in different temperature intervals reflects the formation of different phases, as indicated. (b) Arrhenius plot of σ_{dc} for the data shown in (a) and for analogous data acquired on the stable crystalline phase, both upon heating to above the melting point and cooling through the crystallization transition.

In many H–bonded liquids and supercooled liquids, such as water, monoalcohols, amines and peptides,[46-54] but also liquid EAM,[55] the most intense dielectric loss feature has a symmetric and relatively narrow frequency profile, usually modeled with a Debye or Cole-Cole function (Eq. 1)

and termed “Debye-like” relaxation, which is assigned to a cooperative dynamics of the H-bond network dynamics accompanied by the reorientation of the constituent molecules. The isothermal dielectric loss spectra ε”(*f*) acquired upon heating from the metastable crystal phase are shown in Figure 6(a), where we have merged the low-frequency loss data (a different representation of the data shown in Figure 5(a), see Section 2) with the high frequency data measured in an independent experiment. The high-frequency spectra at high temperature are measured on liquid EAM, and display a relaxation peak in the microwave frequency region (between 10^8 and 10^9 Hz), commonly referred to as “structural relaxation”, whose position is in rough agreement with previous studies.[55,56] This relaxation could be well described by a Cole-Cole function (Eq. 1) with an exponent *c* only slightly lower than unity.

Surprisingly, instead of being featureless, the spectra of the solid phases exhibit three relaxation features, a more intense one at intermediate frequency, which we label as α for reasons to be discussed, and two less intense ones at either side of the latter. The fastest relaxation (the one at highest frequency, labeled as β) has a very low intensity and it is only observed at very low temperatures. It may be noticed that the characteristic frequency of the main (α) loss feature is almost unaffected by the solid-solid transition, and that it changes only slightly upon melting (see inset to Figure 7(a)); at the same time, its intensity (dielectric strength) increases dramatically upon melting: it is higher by more than one order of magnitude in the liquid phase (notice the logarithmic vertical scale in Figure 6(a)). This coincidence of relaxation times suggests that the origin of this main (α) loss is the same in the liquid and solid phases, as we discuss further below. The frequency position and intensity of the α relaxation are also similar in the crystalline metastable and stable phases at a given temperature (169 K in Figure 6(c)).

The characteristic relaxation times of each loss component were extracted by fitting them as the imaginary part of a Cole-Cole function. Concerning the slower (lower-frequency) spectral feature, it can be observed in Figure 6(b) that its relaxation time has virtually the same dependence as the conductivity in both crystal phases, and displays the same discontinuity as σ_{dc} at the solid-solid transition. Hence the origin of this relaxation feature is a space-charge effect due to accumulation of charge at sample heterogeneities such as grain boundaries, which may be expected in a polycrystalline sample obtained by recrystallization from the supercooled liquid or by solid-solid transformation, but whose precise origin in the EAM case will be apparent in what follows. The correlation between the relaxation time of such charge-related loss and the dc conductivity is known as Barton–Nakajima–Namikawa (BNN) condition;[57,58] relaxations fulfilling the BNN condition are often observed in partially conducting disordered materials and organic systems.[59,60]

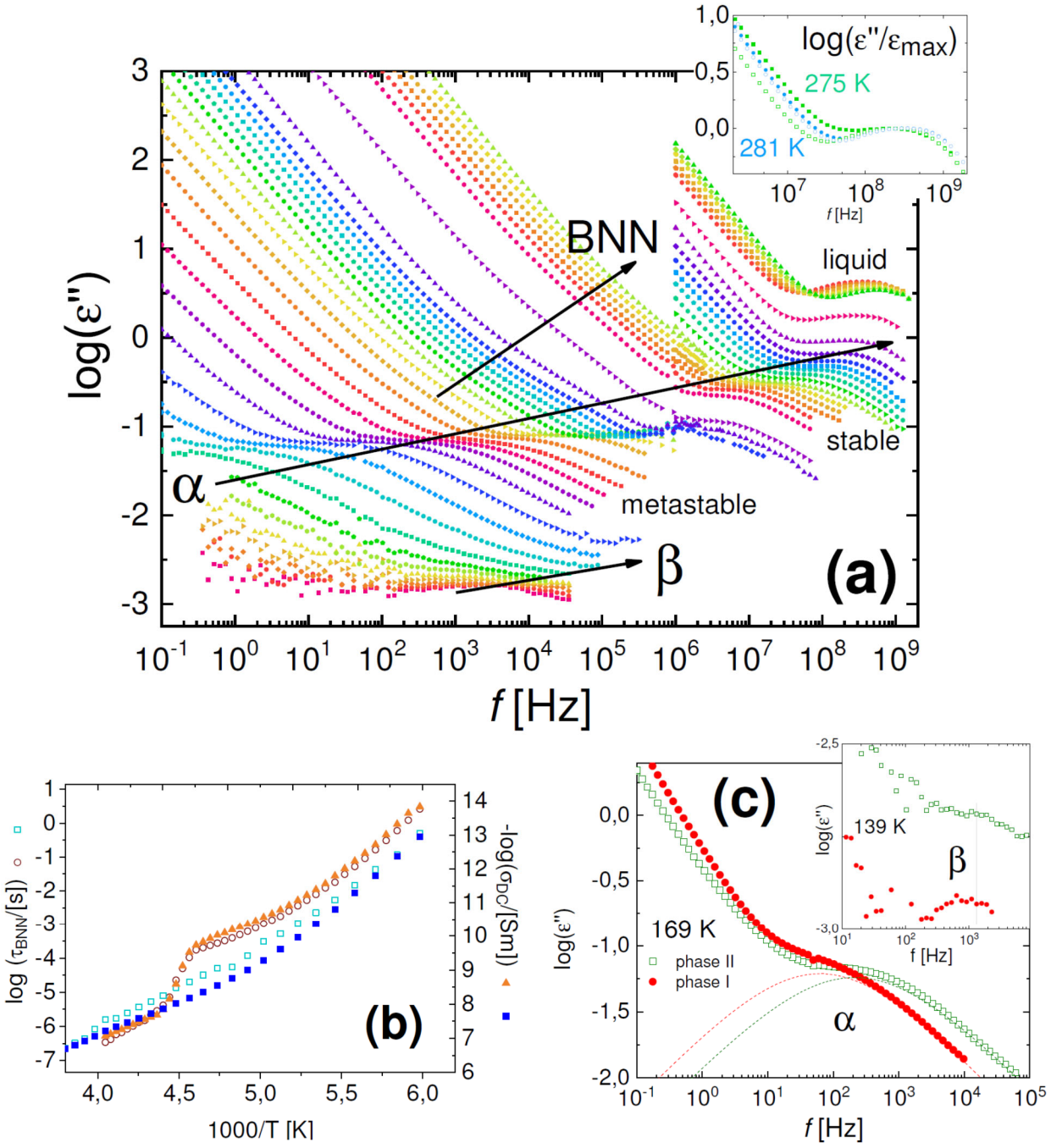

Figure 6. Dielectric loss spectra at different temperatures, acquired while warming up from the metastable crystal phase II. Discontinuities are observed through the transitions from the metastable to stable crystal, and upon melting of the latter phase. Inset: high-frequency loss spectra near the melting point of the stable phase I, normalized to the intensity of the loss peak. (b)

Arrhenius plot of the relaxation time of the prepeak (open markers) across the transition between the metastable and stable phases and in the stable phase, and comparison with that of the dc conductivity in the same temperature range (filled markers). (c) Comparison between the low-frequency loss spectra of the stable and metastable crystalline phases at 169 (main panel) and 139 K (inset).

The relaxation times τ_α and dielectric strength of the main loss in both crystal phases and in the liquid are shown with in panels (a) and (b) of Figure 7, respectively. The smooth temperature dependence of τ_α, which contrasts with the abrupt changes by almost displayed by both σ_{dc} and τ_{BNN}, rules out a possible space-charge origin and points to a dipolar origin of the α relaxation (in fact, the increment of τ_α has opposite sign than that σ_{dc} at both phase changes). Structural relaxations corresponding to molecular reorientation dynamic process are observed in liquids but also in some disordered solids, such as plastic crystals[33] or rotator phases,[61] orientationally disordered crystals,[62] and Condis crystals with dynamic conformational disorder.[63] Since the α relaxation is visible in both the metastable phase and the fully ordered stable one, it cannot be ascribed to the dynamic H-bond disorder that we have observed in the metastable phase II. We can also rule out an origin related to the migration of H–bond defects (missing H–bonds) such as that reported in liquid water and ice,[46,51] as in the case of H_2O it is observed that the relaxation frequency for this process increases by six orders of magnitude upon crossing the melting transition,[50] while in the EAM case there is barely any change in relaxation frequency upon melting (see inset to Figure 6(a)).

We thus conclude that the α relaxation feature observed in the low temperature EAM spectra is not intrinsic to the crystalline phases of this material, and it is instead due to a fraction of the sample that does not crystallize and remains in a supercooled liquid state. Looking at Figure 7(a),

it appears that the main relaxation feature in the solid phases follows the temperature dependence of the structural relaxation in liquid EAM, which could be expected if the former was the structural relaxation of a supercooled liquid fraction. The dielectric strength of the α relaxation, which is proportional to the density of relaxing units,[32] is significantly lower in the crystal phases than in the liquid, consistent with the proposed scenario. The ratio of the dielectric strengths between the low temperature crystal phases and the liquid phase at the melting point (Figure 7(b)), as extracted directly from our fit procedure, indicates that the crystal phases contain between 3% and 7% of supercooled liquid. In both crystal phases, the structural relaxation time of the supercooled liquid fraction displays a small deviation from the Arrhenius behavior, exhibiting a slight curvature in the Arrhenius plot that is typical of the structural relaxation time of kinetically strong glass forming materials.[32] The slightly lower onset melting temperature of the stable crystal phase observed in our study might be a consequence of the heterogeneous sample morphology.

The failure of a fraction of the EAM sample to crystallize is reminiscent of the behavior of other H-bonded liquids. In the case of glycerol, a sample recrystallized from the supercooled liquid state was reported to undergo incomplete crystallization with a final amorphous fraction of about 1%,[64] a value smaller than that obtained here for EAM. An extreme example is that of *n*-butanol, where the amorphous fraction at the end of the crystallization process is reported to be as high as 20 or 30%,[65] although the origin of this effect is likely different than for EAM. The relatively low value of the amorphous fraction in EAM (this study) and glycerol[64] suggests that the amorphous regions are limited in both cases to the boundaries of crystallites that occupy almost the totality of the sample's volume.

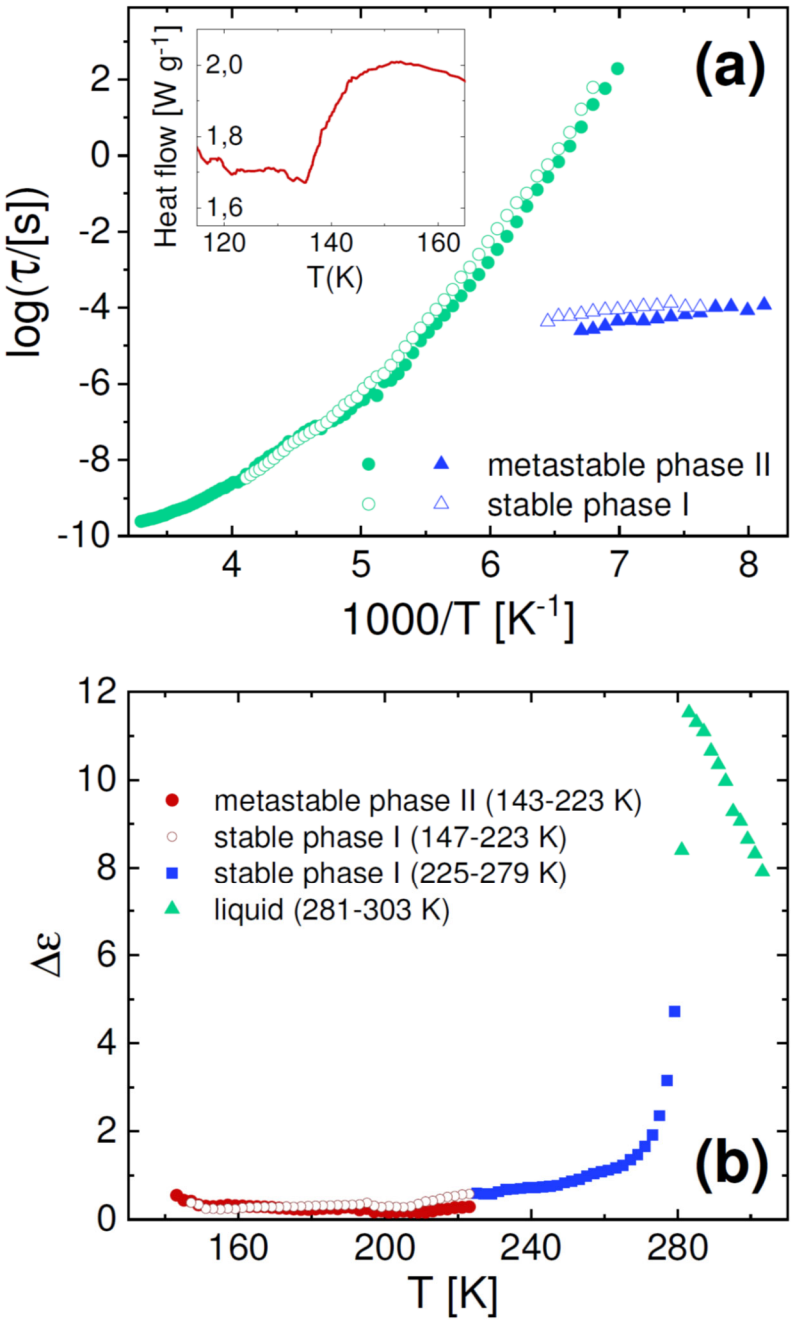

Figure 7. (a) Arrhenius plot of the relaxation times of dipolar relaxations in all EAM phases (data of Figure 6(a) and additional data acquired on the stable crystal phase at low temperature). Circles: α relaxation. Triangles: β relaxation. Filled markers are data for the metastable crystal phase, open markers are the data for the stable (crystal and liquid) phases. Inset: calorimetry thermogram

measured upon heating from the metastable crystal phase of EAM at 10 K min^{-1}. (b) Temperature dependence of the dielectric strength of the α relaxation in all three EAM phases.

As mentioned above, in addition to the BNN and α relaxations a third, weak relaxation feature (β) is present at lower temperature (Figure 6(a,c)), where the amorphous EAM fraction is close to the glass transition. The fact that this relaxation is observed (at basically the same characteristic frequency, see Figure 7(a) and the inset to Figure 6(c)) in both crystal phases, and that it has a shorter characteristic time than the α relaxation indicates that it corresponds to a secondary relaxation of the EAM glass former, likely associated with conformational interconversion dynamics. Instead, no characteristic relaxation feature is observed in the metastable phase that could correspond to the dynamic statistical disorder of the H-bonding groups discussed in Section 3.1. It could be that the associated change in polarization is too weak to be detected, or else that such H-bond dynamics is too fast to be observed in our experimental window. Indeed, our MD simulations suggest that the dipole-dipole correlation decay time in the metastable crystal phase is smaller than 10^{-6} s at 100 K, and due to thermal activation it is expected to be even shorter at the lowest temperatures reachable with our setup (120 K).

The vitrification temperature of the α relaxation, defined as the temperature at which the relaxation times reaches 100 s, were found to be ca. 146 and 145 K for the amorphous fraction of the stable and metastable crystal phases of EAM, respectively. The inset to Figure 7(a) displays a low-temperature scanning calorimetry thermogram acquired on heating the metastable phase. A very subtle step-like increase in the heat flow (and thus an increase in specific heat), similar to that signaling the glass transition of supercooled liquids, is observed at about 140 K, which coincides roughly with the vitrification temperature of the α relaxation, confirming our interpretation. We therefore conclude that the temperature of 140-145 K is a good estimate for the glass transition

temperature (T_g) of liquid EAM. A homogeneous glass state of EAM cannot be reached, at least at our cooling rate, because EAM crystallizes (for the most part) well before T_g is reached; only small liquid domains survive amidst the crystallites, and the T_g under such confinement condition is likely slightly different than it would be in a homogeneous bulk supercooled liquid. A similar situation occurs for water, another liquid with very high H–bond density and which cannot be supercooled by more than 40 K without crystallizing, and whose glass transition can only be observed by film deposition on low-temperature substrates or under nanoconfinement.[66]

In strongly associating H–bonding systems such as liquid EAM, the structural relaxation must involve the breaking and formation of H–bonds;[46,48,52] hence the structural α relaxation is associated with the H–bond network dynamics. As visible in the inset to Figure 6(a), the characteristic frequency of the α relaxation in the bulk liquid near the melting point is slightly lower than in the amorphous fraction surrounding the crystallites of the stable crystal phase. A similar slight difference in relaxation time is observed between the stable and metastable crystal phases (see Figures 6(c) and 7(a)). These differences show that the Debye-like relaxation of H–bonded liquids depends in a nontrivial way on the sample's heterogeneities. In particular, the fact that the α dynamics is faster under confinement than in the bulk liquid is contrary to what might be expected for a reorientational relaxation in the presence of strong interfacial interactions with fully ordered crystalline domains. Further studies in controlled geometries would be needed to investigate in more detail interfacial effects on the Debye-like H–bond rearrangement dynamics.

4. Conclusions.

To summarize, X-ray diffraction, scanning calorimetry, broadband dielectric spectroscopy and molecular dynamics characterization of ethanolamine shows that this strongly associating molecule displays structural polymorphism, with the existence of a metastable monoclinic crystal

phase besides the stable crystalline phase reported in earlier studies,[24] and with an only partial crystallization that leads to the presence of a minority supercooled liquid phase in both crystal phases. While slow cooling from the liquid results in the formation of the stable crystal phase, the metastable one is obtained by fast cooling the liquid at a rate of 10 K min^{-1} to below the crystallization temperature of the stable crystal phase. The metastable phase appears to be characterized by a dynamic statistical disorder of the orientation of the H–bonding moieties. By heating to above ca. 210 K, the metastable crystal phase transforms irreversibly into the thermodynamically stable phase, which then melts between 277 and 281 K. The temperature dependence of the dc conductivity of both solid phases exhibits super-Arrhenius dependence, which is more typical of disordered systems than crystalline ion conductors, and likely corresponds to the diffusion of ionic charge carriers. Dielectric results indicate that a small fraction (ca. 5%) of the sample remains in the supercooled liquid state upon (partial) crystallization. The persistence of the liquid fraction at low temperatures allows estimating the glass transition temperature of liquid EAM, which is found to be around 145 K. Near the melting point, the structural relaxation dynamic is faster in the amorphous fraction of the (semi)crystalline material than in the bulk liquid.

ASSOCIATED CONTENT

Supporting Information. CIFs files for the Rietveld refinement of the powder XRD data of the metastable crystal phases of EAM at 100 K, and of the stable crystal phase at 250 K. The following files are available free of charge.

Ethanolamine_metastable_Rietveld100K.cif

Ethanolamine_stable_Rietveld250K.cif

AUTHOR INFORMATION

Corresponding Author

* Tel: +34 934016568. E-mail: roberto.macovez@upc.edu.

Present Addresses

† Current address: Departament de Física de la Matèria Condensada, Facultat de Física, Av. Martí i Franquès 1, E-08028 Barcelona, Spain.

Author Contributions

The manuscript was written through contributions of all authors. All authors have given approval to the final version of the manuscript.

ACKNOWLEDGMENT

This work has been supported by the Spanish Ministry MINECO through project FIS2017-82625-P and by the Generalitat de Catalunya under project 2017SGR-42.

ABBREVIATIONS

EAM, ethanolamine; BDS, broadband dielectric spectroscopy.

REFERENCES

1. Ball, P. Water as an Active Constituent in Cell Biology. *Chem. Rev.* **2008**, *108*, 74−108

2. Knight, C.; Voth, G. A. The Curious Case of the Hydrated Proton. *Acc. Chem. Res.* **2012**, *45*, 101–109

3. Mallamace, F.; Corsaro, C.; Mallamace, D.; Vasi, S.; Vasi, C.; Baglioni, P.; Buldyrev, S.V.; Chen, S.-H.; Stanley, H.E. Energy Landscape in Protein Folding and Unfolding. *Proc. Natl. Acad. Sci. USA* **2016**, *113*, 3159–3163.

4. Levy, Y.; Onuchic, J. N. Water Mediation in Protein Folding and Molecular Recognition. Annu. Rev. Biophys. Biomol. Struct. 2006, 35, 389−415

5. Tamarit, J. Ll.; Barrio, M.; López, D. O.; Haget, Y. Packing Disordered Molecular Crystals and their Molecular Alloys. *J. Appl. Cryst.* **1997**, *30*, 118–122

6. Salud, J.; Barrio, M.; López, D. O.; Tamarit, J. Ll.; Alcobé, X. Anisotropy of Intermolecular Interactions from the Study of the Thermal-Expansion Tensor. *J. Appl. Cryst.* **1998**, *31*, 748–757

7. Li, J.; Liu, Y.; Zhang, Y.; Cai, H.-L.; Xiong, R.-G. Molecular Ferroelectrics: Where Electronics Meet Biology. *Phys. Chem. Chem. Phys.* **2013**, *15*, 20786–20796

8. Tayi, A. S.; Kaeser, A.; Matsumoto, M.; Aida, T.; Stupp, S. I. Supramolecular Ferroelectrics. *Nat. Chem.* **2015**, *7*, 281–294

9. Newnham, R.E.; Cross, L.E. Ferroelectricity: The Foundation of a Field from Form to Function. *MRS Bull.* **2005***, 30*, 845–846

10. Agmon, N. The Grotthuss Mechanism. *Chem. Phys. Lett.* **1995**, *244*, 456–462

11. Agmon, N.; Bakker, H.J.; Campen, R.K.; Henchman, R.H.; Pohl, P.; Roke, S.; Thämer, M.; Hassanali, A. Protons and Hydroxide Ions in Aqueous Systems. *Chem. Rev.* **2016**, *116*, 7642−7672

12. Capelli, S. C.; Falvello, L. R.; Forcén-Vázquez, E.; McIntyre, G. J.; Palacio, F.; Sanz, S.; Tomás, M. Proton Cascade in a Molecular Solid: H/D Exchange on Mobile and Immobile Water. *Angew. Chem. Int. Ed.* **2013**, *52*, 13463–13467

13. Zachariah, M.; Mitsari, E.; Romanini, M.; Zygouri, P.; Gournis, D.; Barrio, M.; Tamarit, J.Ll.; Macovez, R. Water-Triggered Conduction Mediated by Proton Exchange in a Hygroscopic Fulleride and its Hydrate. *J. Phys. Chem. C* **2015**, *119*, 685–694

14. Mitsari, E.; Romanini, M.; Barrio, M.; Tamarit, J. Ll.; Macovez, R. Protonic Surface Conductivity and Proton Space-Charge Relaxation in Hydrated Fullerol. *J. Phys. Chem. C* **2017**, *121*, 4873–4881

15. Bernardes, C. E. S.; Matos Lopes, M. L. S.; Ascenso, J. R.; Minas da Piedade, M. E. From Molecules to Crystals: The Solvent Plays an Active Role Throughout the Nucleation Pathway of Molecular Organic Crystals. *Cryst. Growth Des.* **2014**, *14*, 5436−5441

16. Nicolaï, B.; Itié, J.-P.; Barrio, M.; Tamarit, J. Ll.; Rietveld, I. B. Thermodynamics by Synchrotron X-Ray Diffraction: Phase Relationships and Crystal Structure of L-Tyrosine Ethyl Ester Form III. *Cryst. Eng. Comm.* **2015**, *17*, 3974–3984

17. Allouchi, H.; Nicolaï, B.; Barrio, M.; Céolin, R.; Mahé, N.; Tamarit, J. Ll.; Do, B.; Rietveld, I. B. On the Polymorphism of l-Citrulline: Crystal Structure and Characterization of the Orthorhombic δ Form. *Cryst. Growth Des.* **2014**, *14*, 1279−1286

18. Mahé, N.; Nicolaï, B.; Barrio, M.; Perrin, M.-A.; Do, B.; Tamarit, J. Ll.; Céolin, R.; Rietveld, I. B. Solid-State Properties and Dehydration Behavior of the Active

Pharmaceutical Ingredient Potassium Guaiacol-4-sulfonate. *Cryst. Growth Des.* **2013**, *13*, 3028–3035

19. Desiraju, G. R. Crystal Engineering: A Holistic View. *Angew. Chem. Int. Ed.* **2007**, *46*, 8342–8356

20. Zhu, L.; Schade, G. W.; Nielsen, C. J. Real-time monitoring of emissions from monoethanolamine-based industrial scale carbon capture facilities. *Environ. Sci. Technol.* **2013**, *47*, 14306−14314

21. Lv, B.; Guo, B.; Zhou, Z.; Jing, G. Mechanisms of CO2 Capture into Monoethanolamine Solution with Different CO2 Loading during the Absorption/Desorption Processes. *Environ. Sci. Technol.* **2015**, *49*, 10728–10735

22. Räsänen, M.; Aspiala, A.; Homanen, L.; Murto, J. IR-Induced Photorotamerization of 2-Aminoethanol in Low-Temperature Matrices. Ab Initio Optimized Geometries of Conformers. *J. Mol. Struct.* **1982**, *96*, 81–100

23. Silva, C. F. P.; Duarte, M. L. T. S.; Fausto, R. A. Concerted SCF-MO Ab Initio and Vibrational Spectroscopic Study of the Conformational Isomerism in 2-Aminoethanol. *J. Mol. Struct.* **1999**, *482–483*, 591–599

24. Mootz, D.; Brodalla, D.; Wiebke, M. Structures of Monoethanolamine (MEAM), Diethanolamine (DEAM) and Triethanolamine (TEAM). *Acta Cryst. C* **1989**, *45*, 754–757

25. Hess, B.; Kutzner, C.; van der Spoel, D.; Lindahl, E. GROMACS 4: Algorithms for Highly Efficient, Load-Balanced, and Scalable Molecular Simulation. *J. Chem. Theory Comput.* **2008**, *4*, 435–447

26. Caleman, C.; van Maaren, P. J.; Hong, M.; Hub, J. S.; Costa L. T.; van der Spoel, D. Force Field Benchmark of Organic Liquids: Density, Enthalpy of Vaporization, Heat Capacities, Surface Tension, Isothermal Compressibility, Volumetric Expansion Coefficient, and Dielectric Constant. *J. Chem. Theory Comput.* **2012**, *8*, 61–74

27. Jorgensen, W. L.; Tirado-Rives, J. Potential Energy Functions for Atomic-Level Simulations of Water and Organic and Biomolecular Systems. *Proc. Natl. Acad. Sci. U.S.A.* **2005**, *102*, 6665–6670

28. Cardona, J.; Fartaria, R.; Sweatman, M. B.; Lue, L. Molecular Dynamics for the Prediction of the Dielectric Spectra of Alcohols, Glycols and Monoethanolamine. *Mol. Sim.* **2016**, *42*, 370−390

29. The program ANGULA can be downloaded at https://gcm.upc.edu/en/members/luis-carlos/angula/ANGULA

30. Tripathi, P.; Gonzalo-Ruiz, J.; Mitsari, E.; Zachariah, M.; Romanini, M.; Tamarit, J. Ll.; Muñoz, F. X.; Macovez, R. Silicon-Chip-Based Dielectric Spectroscopy for Conductivity and Molecular Dynamics Studies of Organic Films. *J. Phys. Chem. Lett.* **2014**, *5*, 2796−2801

31. Zachariah, M.; Romanini, M.; Tripathi, P.; Tamarit, J.Ll.; Macovez, R. Molecular Diffusion and Dc Conductivity Perfectly Correlated with Molecular Rotational Dynamics in a Plastic Crystalline Electrolyte. *Phys. Chem. Chem. Phys.* **2015**, *17*, 16053–16057.

32. Kremer, F.; Schönhals, A. Broadband Dielectric Spectroscopy. Springer: Berlin, 2003.

33. Zachariah, M.; Romanini, M.; Tripathi, P.; Barrio, M.; Tamarit, J.Ll.; Macovez, R. Self-Diffusion, Phase Behavior, and Li^+ Ion Conduction in Succinonitrile-Based Plastic Co-Crystals. *J. Phys. Chem. C* **2015**, *119*, 27298–27306

34. Cole, K.S.; Cole, R.H. Dispersion and Absorption in Dielectrics – I. Alternating Current Characteristics. *J. Chem. Phys.* **1941**, *9*, 341–352

35. Penn, R. E.; Curl Jr., R. F. Microwave Spectrum of 2-Aminoethanol: Structural Effects of the Hydrogen Bond. *J. Chem. Phys.* **1971**, *55*, 651

36. da Silva, E. F.; Kuznetsova, T.; Kvamme, B.; Merz Jr, K. M. Molecular Dynamics Study of Ethanolamine as a Pure Liquid and in Aqueous Solution. *J. Phys. Chem. B* **2007**, *111*, 3695–3703

37. Novakovskaya, Y. V.; Rodnikova, M. N. Ethanolamine: Conformational Diversity. *Struct. Chem.* **2015**, *26*, 177–187

38. Smith, T. D.; Gerken, J. B.; Jog, P. V.; Roberts, J. D. Conformational Equilibria of Ethanolamine and Its Hydrochloride in Solution. *Org. Lett.* **2007**, *9*, 4555–4557

39. Haynes, W. M. (Ed.). CRC Handbook of Chemistry and Physics. 95th Edition. CRC Press LLC, Boca Raton (US), 2014, p. 3–246

40. MS Modeling (Materials Studio), version 5.5. Available at: http://accelrys.com/products/collaborative-science/biovia-materials-studio.

41. Romanini, M.; Negrier, Ph.; Tamarit, J. Ll.; Capaccioli, S.; Barrio, M.; Pardo, L. C.; Mondieig, D. Emergence of Glassy-Like Dynamics in an Orientationally Ordered Phase. *Phys. Rev. B* **2012**, *85*, 134201

42. Negrier, Ph.; Barrio, M.; Romanini, M.; Tamarit, J. Ll.; Mondieig, D; Krivchikov, A. I.; L. Kepinski, L.; Jezowski, A.; Szewczyk, D. Polymorphism of 2-Adamantanone. *Cryst. Growth Des.* **2014**, *145*, 2626-2632

43. Do, C.; Lunkenheimer, P.; Diddens, D.; Gotz, M.; Weiss, M.; Loidl, A.; Sun, X.G.; Allgaier J.; Ohl, M. Li+ Transport in Poly(Ethylene Oxide) Based Electrolytes: Neutron Scattering, Dielectric Spectroscopy, and Molecular Dynamics Simulations. *Phys. Rev. Lett.* **2013**, 111, 018301

44. Charalampopoulos, V. G.; Papaioannou, J. C. Dipole Relaxation and Proton Transport in Polycrystalline γ-Cyclodextrin Hydrate: A Dielectric Spectroscopy Study. *Solid State Ionics* **2011**, *191*, 1–11

45. Wojnarowska, Z.; Wang, Y.; Paluch, K. J.; Sokolov, A. P.; Paluch, M. Observation of Highly Decoupled Conductivity in Protic Ionic Conductors. *Phys. Chem. Chem. Phys.* **2014**, *16*, 9123–9127

46. Popov, I.; Ishai, P. B.; Khamzin, A.; Feldman, Y. The Mechanism of the Dielectric Relaxation in Water. *Phys. Chem. Chem. Phys.* **2016**, *18*, 13941–13953

47. Elton, D. C. The Origin of the Debye Relaxation in Liquid Water and Fitting the High Frequency Excess Response. *Phys. Chem. Chem. Phys.* **2017**, *19*, 18739–18749

48. Kaatze, U. Dielectric and Structural Relaxation in Water and Some Monohydric Alcohols. *J. Chem. Phys.* **2017**, *147*, 024502

49. Gainaru C.; Kastner, S.; Mayr, F.; Lunkenheimer, P.; Schildmann, S.; Weber, H. J.; Hiller, W.; Loidl, A.; Böhmer, R. Hydrogen-Bond Equilibria and Life Times in a Supercooled Monohydroxy Alcohol. *Phys. Rev. Lett.* **2011**, *107*, 118304

50. Artemov, V. G.; Volkov, A. A. Water and Ice Dielectric Spectra Scaling at 0 °C. *Ferroelectrics* **2014**, *466*, 158

51. Popov, I.; Puzenko, A.; Khamzin, A.; Feldman, Y. The Dynamic Crossover in Dielectric Relaxation Behavior of Ice I_h. *Phys. Chem. Chem. Phys.* **2015**, *17*, 1489–1497

52. Böhmer, R.; Gainaru, C.; Richert, R. Structure and Dynamics of Monohydroxy Alcohols—Milestones Towards Their Microscopic Understanding, 100 Years after Debye. *Phys. Rep.* **2014**, *545*, 125–195

53. Gainaru C.; Bauer, S.; Vynokur, E.; Wittkamp, H.; Hiller, W.; Richert, R.; Böhmer, R. Dynamics in Supercooled Secondary Amide Mixtures: Dielectric and Hydrogen Bond Specific Spectroscopies. *J. Phys. Chem. B* **2015**, *119*, 15769

54. Lunkenheimer, P.; Emmert, S.; Gulich, R.; Köhler, M.; Wolf, M.; Schwab, M.; Loidl, A. Electromagnetic-Radiation Absorption by Water. *Phys. Rev. E* **2017**, *96*, 062607

55. Patil, A. V.; Pawar, V. P. Microwave Dielectric Spectra and Molecular Interaction in a Binary Mixture of Ethanolamine with Diethanolamine. *J. Mol. Liq.* **2013**, *188*, 1–4

56. Patil, A. V.; Shinde, G. N.; Pawar, V. P. Dielectric Relaxation Study of Hydrogen Bonded Structures in Ethanolamine with Diethanolamine Using TDR Technique. *J. Mol. Liq.* **2012**, *168*, 42–46

57. Namikawa, H. Characterization of the Diffusion Process in Oxide Glasses Based on the Correlation between Electric Conduction and Dielectric Relaxation. *J. Non-Cryst. Solids* **1975**, *18*, 173

58. Yamamoto K.; Namikawa, H. Conduction Current Relaxation of Inhomogeneous Conductor I. *Jpn. J. Appl. Phys. Part 1* **1988**, *27*, 1845

59. Jonscher, A. K. The 'Universal' Dielectric Response. *Nature* **1977**, *267*, 673.

60. Macovez, R.; Zachariah, M.; Romanini, M.; Zygouri, P.; Gournis, D.; Tamarit, J.Ll. Hopping Conductivity and Polarization Effects in a Fullerene Derivative Salt. *J. Phys. Chem. C* **2014**, *118*, 12170−12175

61. Macovez, R.; Goldoni, A.; Petaccia, L.; Marenne, I.; Brühwiler, P.A.; Rudolf, P. Reversible Phase Transformation and Doubly Charged Anions at the Surface of Simple Cubic RbC60. *Phys. Rev. Lett.* **2008**, *101*, 236403

62. Tripathi, P.; Mitsari, E.; Romanini, M.; Serra, P.; Tamarit, J. Ll.; Zuriaga, M.; Macovez, R. Orientational Relaxations in Solid (1,1,2,2)Tetrachloroethane. *J. Chem. Phys.* **2016**, *144*, 164505

63. Romanini, M.; Mitsari, E.; Tripathi, P.; Serra, P.; Zuriaga, M.; Tamarit, J. Ll.; Macovez, R. Simultaneous Orientational and Conformational Molecular Dynamics in Solid 1,1,2-Trichloroethane. *J. Phys. Chem. C* **2018**, *122*, 5774−5783

64. Sanz, A.; Niss, K. Liquid Dynamics in Partially Crystalline Glycerol. *J. Chem. Phys.* **2017**, *146*, 044502

65. Wypych, A.; Guinet, Y.; Hédoux, A. Isothermal Transformation of Supercooled Liquid n-Butanol near the Glass Transition: Polyamorphic Transitions in Molecular Liquids Investigated using Raman Scattering. *Phys. Rev. B* **2007**, *76*, 144202

66. Angell, C. A. Insights into Phases of Liquid Water from Study of Its Unusual Glass-Forming Properties. *Science* **2008**, *319*, 582–587

SYNOPSIS

A simple ethane derivative, ethanolamine, is found to exhibit a metastable crystal phase that can be obtained from the supercooled liquid phase. The crystallization is frustrated, with 5% of the sample remaining amorphous also after transformation to the stable crystal phase. The metastable phase appears to be characterized by a dynamic statistical disorder of the H–bonding groups.